Macromolecules ARTICLE

Macromolecules **2010**, *43*, 8153–8161 **8153**
DOI: 10.1021/ma101213h

Probing the Chain and Crystal Lattice Orientation in Polyethylene Thin Films by Near Edge X-ray Absorption Fine Structure (NEXAFS) Spectroscopy

Yantian Wang,*,[†] Ying Zou,[‡,⊥] Tohru Araki,[‡,#] Jan Lüning,[§,▽] A. L. D. Kilcoyne,[∥] Jonathan Sokolov,[†] Harald Ade,[‡] and Miriam Rafailovich[†]

[†]*Department of Materials Science and Engineering, Stony Brook University, Stony Brook, New York 11794-2275,* [‡]*Department of Physics, North Carolina State University, Raleigh, North Carolina 27695,* [§]*Stanford Synchrotron Radiation Lightsource, Stanford, California 94209, and* [∥]*Advanced Light Source, Berkeley National Laboratory, Berkeley, California 94720.* [⊥] *Present address: Department of Physics, University of Wisconsin—Milwaukee, Milwaukee, WI 53211.* [#] *Present address: Toyota Central R&D Laboratories., Inc. Japan.* [▽] *Present address: Laboratoire de Chimie Physique, Université Pierre et Marie Curie, 75005 Paris, France.*

Received May 31, 2010; Revised Manuscript Received August 17, 2010

ABSTRACT: The chain and the crystal unit cell orientation of linear low density polyethylene (LLDPE) were measured with near edge X-ray absorption fine structure (NEXAFS) spectroscopy. A strongly attractive substrate, silicon, and a weakly attractive substrate, mica, were used. For a 100 nm thick LLDPE film on the silicon substrate, the crystals exhibit an edge-on lamellar morphology, with the chains predominantly parallel to the substrate, and the orthorhombic unit cell $\langle a, b, c\rangle$ in the following approximate orientation: b and c are in the film plane with b along the crystal fibril direction and c perpendicular to the fibril direction and a perpendicular to the film plane. On the mica substrates, LLDPE films with thickness below 180 nm completely dewet the surface and form isolated droplets, while a film 366 nm thick crystallizes as spherulites with most of the chains perpendicular to the substrate before annealing and with a twisted lamellar structure after isothermal crystallization at 60 °C. The results demonstrate that the combination of electron yield NEXAFS and high spatial resolution transmission NEXAFS is a powerful tool to measure the crystal orientation in the polymer thin films on a small length scale.

Introduction

Semicrystalline polymer thin films have attracted great interest due to their increasingly important role in microelectronics,[1] organic photovoltaic cells,[2] the coating industry, substrates for organic electronic devices,[3] and optical insulating layers.[4] The chain orientation in the polymer thin films is one of the key parameters that determine their mechanical, optical, adhesive, and electronic properties.

In our previous work, we studied crystallization and melting of the thin and ultrathin films of linear low density polyethylene (LLDPE) and found that the morphology, lamellar orientation, and melting temperature depend strongly on the film thickness and the substrate interaction.[5,6] We also showed that, on silicon substrate, the chain orientation in films thinner than 30 nm was different from that in films thicker than 30 nm.[6] However, the orientation of the polymer chains on different substrates and the orientation of the crystal unit cells are not well-understood. Traditionally, the orientation of the crystal unit cells in thin polymer single crystals crystallized from dilute solutions is measured by electron diffraction.[7] However, due to the inelastic interactions between irradiating electrons and the long-chain molecules in polymers, the crystalline structure of the polymers degenerates and disappears very quickly upon exposure to the electron beam, although the morphology of the crystals remains unchanged.[8] So this technique usually requires metal coatings on the polymer crystals to prevent electron radiation damage to the crystal, and consequently, the diffraction from the metals imposes interference to the diffraction patterns from the polymer. Direct determination of the orientation of the chains and the crystal lattice in the polymers, either in single crystal form or in the semicrystal form, calls for new methodologies. Despotopoulou et al. successfully measured the chain orientation in an ultrathin film of poly(di-*n*-hexylsilane) with respect to the film surface using transmission and grazing incidence reflectance−Fourier transformed infrared spectroscopy.[9] However, precise measurement of the chain orientation on a fine scale and the orientation of the crystal unit cells in the polymers still remain a big challenge. With the development of modern technologies, more options are emerging. As a powerful surface structure analytic tool, near edge X-ray absorption fine structure (NEXAFS) spectroscopy has proven to be a precise method to explore the chain orientation in polymers or self-assembled monolayers of small organic molecules near the surface.[10−20] Weiss et al., by studying the highly ordered Langmuir−Blodgett films of Ca-arachidate, commented on the importance of matrix effects in these systems.[21] Stöhr et al. found that, in the highly orientated polyethylene, the C−H resonance exhibits the largest signal when the electric field vector **E** is perpendicular to the chain direction, i.e. in the plane of C−H bonds, and hence the angular dependence of the C−H resonance on the hydrocarbon opened a new avenue for NEXAFS studies of the chain orientation in the polymers.[22] Ohta et al. also demonstrated the polarization dependence of C−H and C−C peaks in the PE films and several other polymers.[23] Schöll et al., in studying the ethylene-1-alkene copolymers with various concentrations of

---

*Corresponding author. E-mail: ytwang@notes.cc.sunysb.edu, yttwang@gmail.com. Phone: (631)-632-8467. Fax: (631)-632-5764.

© 2010 American Chemical Society

Published on Web 09/02/2010

side chains, reported that the appearance of a split peak near the C−H resonance (288 eV) peak energy was directly correlated to the crystallinity of the polymer, a result of a special form of a matrix and configuration effects in the NEXAFS of polyethylene.[24] Later on, Zou et al. reported the relationship between the intensity of these two low energy peaks and the *a* and *b* axis orientation in single crystals of *n*-tetracontane. It was shown that the 287.5 eV and 288.2 eV peaks exhibit a maximum and minimum when **E** was aligned along *b* and perpendicular to *a*, respectively. The two spectral features at different energies have their dipole transition moments in orthogonal directions. This, in combination with the dipole transition moment of the C−C resonance orthogonal to the lower energy transition, opens up the feasibility of determining the crystal lattice orientation in polyethylene thin films with NEXAFS, at least qualitatively.[25] The NEXAFS technique has been applied previously in studying the molecular orientation of Kevlar fibers where the phenyl ring orientation within the fiber was clearly demonstrated.[26,27] Castner et al. examined the polymerized tetrafluoroethylene (PTFE) films and revealed the angular dependence of the spectra on the CF_2 chains.[28] Lippitz et al. studied the biaxially stretched and spin-coated PET with the florescence yield NEXAFS and showed the potential of the method to differentiate precisely between partially crystalline and amorphous states at high surface sensitivity.[29] Weiss et al. did a comprehensive study in the chain alignment on the buffed PMDA-ODA (pyromellitimido-oxidianiline) polyimide (PI) surface by NEXAFS and determined the orientational distribution functions of the polymer subunits, their dependence on the buffed strength, as well as the interrelation of the pretilt angles between the liquid crystal and the polyimide alignment layer.[30,31] NEXAFS has also been used to investigate a number of other systems including spider silk fibers.[32,33] Sambasivan et al. measured the molecular orientation of ultrahigh molecular weight polyethylene induced by various sliding motions.[34] However, no work has been reported to date on the complete determination of the crystal lattice orientation in polyethylene by NEXAFS. Moreover, the use of X-ray microscopy in soft materials has the potential to determine the molecular orientation and quantify the sample composition on a fine spatial scale (50 nm) at relatively low damage, which is difficult by other methods.[35,36] In this study, we used silicon and mica substrates, which have high and low affinity, respectively, to LLDPE, and produced and crystallized thin LLDPE films on both substrates. The chain and crystal lattice orientation was determined by NEXAFS with in-plane and out-of-plane sample rotation. We also imaged the films removed from the substrates in transmission NEXAFS mode in a scanning transmission X-ray microscope (STXM) to determine the morphologies and their correspondence to local crystalline orientations. The atomic force microscopy (AFM) images revealed the different morphologies of the films on the two substrates, which confirmed the different substrate interactions with the LLDPE films that played an important role in leading to different chain orientations.

Crystal Lattice Structure of Polyethylene (PE) and NEXAFS Study on PE

The general features of NEXAFS spectra from polymers are characterized by typical peaks near the carbon K-shell excitation in three regions from lower to upper energy: (1) C-1s → π^* resonances, the peaks of which appear at ∼285−286 eV, (2) the C-1s → σ^*_{C-H}/Rydberg resonance peak near 288 eV, and (3) C-1s → σ^*_{C-C} resonances, the peaks of which appear in the 290−295 eV region.[23] For polymers with all saturated hydrocarbons, there are no π transitions, and their spectra consist of peaks from regions 2 and 3 only.[37] PE crystal has orthorhombic unit cells $\langle abc \rangle$ with the *c* axis parallel to the carbon backbone chain and the *a* axis and *b* axis perpendicular to it. The lattice parameters for the linear PE are a = 7.418 Å, b = 4.946 Å, and c = 2.546 Å.[38] In this study, we used the short chain (hexene) branched PE instead of the linear PE. Previous studies have demonstrated that the short chain branched PE also has an orthorhombic unit cell with slightly different lattice parameters depending on the branch length and concentration.[39] Hence, we used X-ray diffraction to confirm the orthorhombic unit cell structure in our samples and calculated the lattice parameters in the bulk PE we used (see Figure 1).

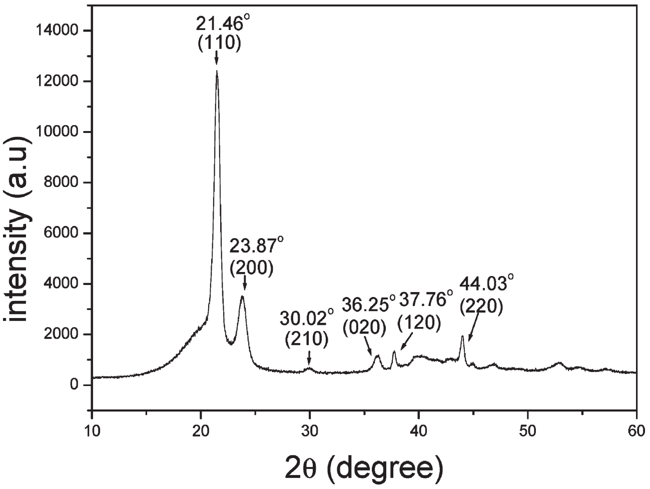

Figure 1. X-ray diffraction profile of the bulk LLDPE.

From the peak positions we confirmed the orthorhombic unit cell and calculated the lattice parameters a = 7.456 Å and b = 4.979 Å, which are slightly larger than those for linear polyethylene, due to the lattice expansion as a consequence of the strain caused by the accumulation of the comonomer on the surface of the crystals.[39]

Previous NEXAFS studies of the PE spectrum showed that the C−H resonance with an absorption peak near the 288 eV region has the polarization direction perpendicular to the C−C chain, and the C−C resonance, the peak of which locates at the 290−295 eV region, has the polarization direction parallel to the C−C chain.[23,40] The study on the ethylene-1-alkene copolymer with controlled composition showed that the split peaks near the 288 eV regions are correlated with the degree of crystallinity, and a blurring of the split peak was observed with the decrease in the crystallinity.[24] From the study of *n*-tetracontane ($C_{40}H_{82}$) single crystals, it has also been demonstrated that a clear relationship between the crystallite orientation and the split peak exists: the intensity of the lower energy peak (287.5 eV) is maximized when $\mathbf{E} \parallel b$, while the higher energy peak (288.2 eV) is maximized when $\mathbf{E} \parallel a$.[25] Since the peaks at the two regions are due to the resonance at a specific direction with respect to the backbone chain, the orientation of the polymer chain and the crystal unit cells can thus be determined from the relevant peaks at various incident angles. Using this principle, the crystal lattice orientation of the PE thin films can be studied. Combined with X-ray transmission images, the chain orientation can be measured at a resolution of 50 nm.

Experimental Section

Materials and Sample Preparation. We used the metallocene catalyzed short chain branched polyethylene with hexene as the comonomer provided by ExxonMobil Research and Engineering Corporation (M_w = 50,000, M_w/M_n = 2, T_m = 117 °C, ρ = 0.92 g/cm^3, branch concentration = 3.3 mol %). Silicon wafers were boiled in the mixture of $H_2SO_4/H_2O_2/H_2O$ (1:1:3 in volume) solution for 2 h and etched in HF/H_2O (1:10 in volume)

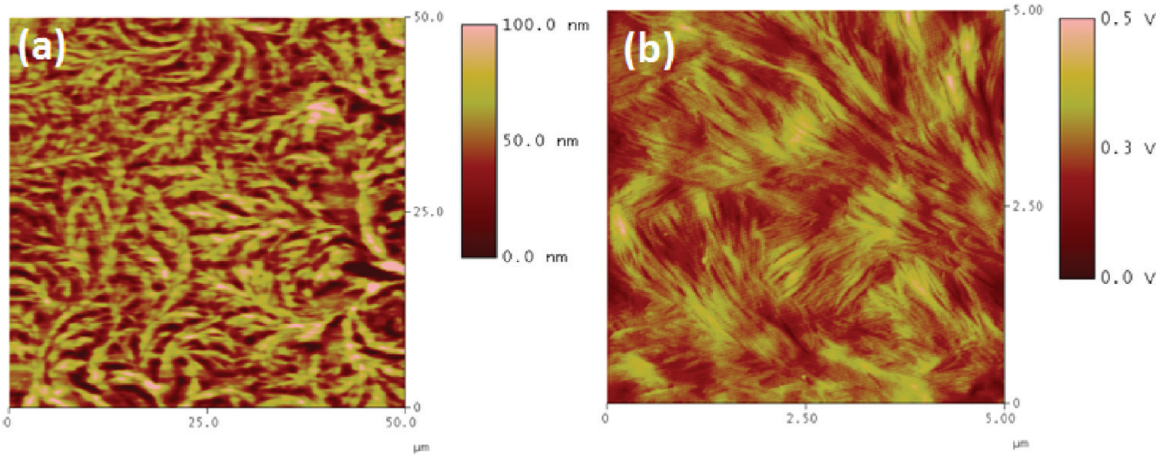

Figure 2. AFM images of nonisothermal crystallized LLDPE (100 nm thick) on a silicon substrate: (a) height image with scan size of 50 × 50 μm^2; (b) lateral force image with scan size of 5 × 5 μm^2.

solution for 30 s right before use as the substrate. This method produced the hydrophobic silicon substrates with an extremely thin (approximately 20 Å) oxide layer on top.[41] Mica substrates were freshly cleaved right before use. PE films were made by spin-coating from the preheated polymer/toluene solution onto preheated substrates. Different thicknesses were obtained by varying the solution concentration (1−30 mg/mL), while the spinning speed was fixed at 2500 rpm. Film thickness was measured with a three-wavelength AutoEL-II ellipsometer (Rudolf Research). Films were then crystallized in the vacuum oven (10 mTorr) using one of the following crystallization processes: (1) a nonisothermal crystallization process, in which the films were heated at 140 °C for 30 min and then gradually cooled to room temperature overnight before exposure to the atmosphere; (2) isothermal crystallization, in which the films were preheated at 140 °C for 30 min and then crystallized at 60 °C overnight. Samples were either used directly for NEXAFS measurement in total electron yield (TEY) mode or were peeled off the substrate in the KOH/H_2O solution at elevated temperature, transferred to clean deionized water, and picked up onto Formvar/carbon coated grids for the scanning transmission X-ray microscopy (STXM) measurement.

Atomic Force Microscopy. The morphology of the films was measured with a Digital Instrument Dimension 3000 atomic force microscope (AFM) in contact mode with a Si_3N_4 tip.

NEXAFS Measurements. The NEXAFS experiments with TEY mode have been carried out at beamline BL-5-2 at the Standford Synchrotron Radiation Lightsource. The beam spot was defocused to about 2 mm by 2 mm in order to avoid any radiation damage. The total yield was registered though the sample current; the intensity of the incoming radiation (I_0) was monitored through the photon current of the Au mesh; the spectra were taken with a grating of groove density 1200 L/m, which is optimized in the range 250−1500 eV with the energy resolution 0.07−1.0 eV. Spectra were calibrated at the energy scale against carbon feature at 284.7 eV in I_0 spectra. All the spectra were normalized at $h\nu = 320$ eV. The STXM measurements were carried out at beamline 5.3.2 of the Advanced Light Source at Lawrence Berkeley National Laboratory. The nominal spatial resolution was about 45 nm.[42]

Results and Discussions

Crystal Lattice Orientation of a 100 nm Thick LLDPE Film Crystallized on Silicon. The morphologies of the LLDPE film with a thickness of 100 nm after nonisothermal crystallization observed with AFM are shown in Figure 2. The height image with the scan size of 50 μm exhibits the curly sheaflike crystal structure. The lateral force image reveals the bundles of edge-on lamellae inside the crystal fibrils.

The chain orientation of this film was measured with the TEY mode. The geometry of the X-ray incidence in the TEY experiment is shown in Figure 3a. The incident angle θ is defined as the angle between the electron vector **E** of the linearly polarized incident X-ray and the surface normal. NEXAFS spectra were acquired at various angles θ, the results of which are shown in Figure 3b. The pronounced C-1s $\rightarrow \sigma^*_{\mathrm{C-H}}$ split peak in the 288 eV region indicates good crystallinity. The intensity of the C-1s $\rightarrow \sigma^*_{\mathrm{C-C}}$ absorption signal near 293 eV increases as θ increases, which indicates that the chains, and consequently the *c* axis, align parallel to the surface. Moreover, the intensity ratio of the lower energy peaks $I_{287.5\mathrm{eV}}/I_{288.2\mathrm{eV}}$ also increases as θ increases, or more specifically, $I_{287.5\mathrm{eV}}$ increases with an increase in θ, while $I_{288.2\mathrm{eV}}$ decreases for an increase in θ. The dependence of the dichroic ratio (DR), which is defined as $(I_{287.5\mathrm{eV}} - I_{288.2\mathrm{eV}})/(I_{287.5\mathrm{eV}} + I_{288.2\mathrm{eV}})$, on θ is plotted in Figure 3c. The resonance intensity for calculating the DR has been taken at the corresponding peak maximum after the spectra have been normalized at $h\nu = 320$ eV. From the monotonic increase of the DR with increasing θ, the increasing tendency of $I_{287.5\mathrm{eV}}/I_{288.2\mathrm{eV}}$ with increasing θ is further confirmed. Considering that $I_{287.5\mathrm{eV}}$ maximizes when $\mathbf{E} \| b$, while $I_{288.2\mathrm{eV}}$ maximizes when $\mathbf{E} \| a$,[25] it can be concluded that *b* orients mostly in the film plane, while *a* tends to lie along the film plane normal.

Locally acquired NEXAFS spectra are more readily interpreted than the TEY NEXAFS spectra that average different crystallite orientations and only a certain depth of the film of ~5−10 nm. Hence, the in-plane and out-of-plane orientation of the bulk crystallite of the same film was measured in transmission with STXM. In this set of experiments, the angle Φ was defined as the angle between the direction of the electric field **E**, i.e. polarization, and the crystal fibril direction (the direction in which the crystal lamellae extends to form the crystal fibril) (Figure 4a).

The transmission NEXAFS spectra of the film taken at different Φ values are shown in Figure 4b. As revealed by the figure, the C-1s $\rightarrow \sigma^*_{\mathrm{C-H}}$ (~288 eV) and the C-1s $\rightarrow \sigma^*_{\mathrm{C-C}}$ (~292.8 eV) resonances have strongly varying and reversed intensities for Φ values of 0° and 90°. As Φ increases, two trends are observed: (1) For $\Phi = 0°$, the ratio $I_{292.8\mathrm{eV}}/I_{288.2\mathrm{eV}} < 1$; with increasing Φ, $I_{292.8\mathrm{eV}}/I_{288.2\mathrm{eV}}$ increases, and it reaches a maximum for $\Phi = 90°$. As $I_{292.8\mathrm{eV}}$ reflects the absorption resonances with the polarization direction along the C−C chain, while $I_{288.2\mathrm{eV}}$ corresponds to the C−H absorption resonance which is perpendicular to the C−C

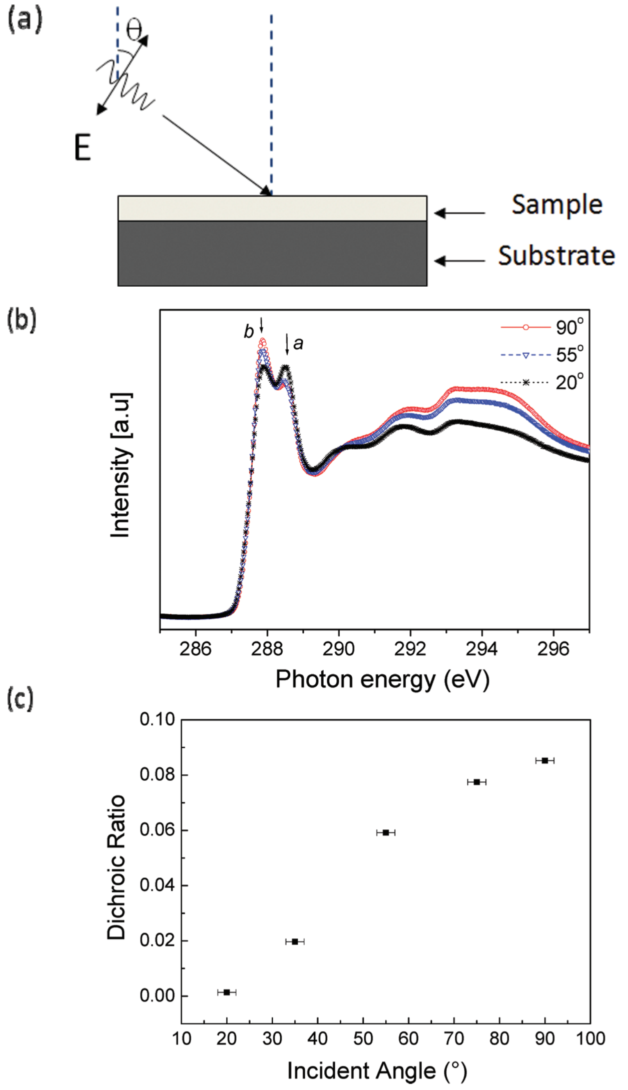

Figure 3. (a) Geometry of the X-ray incident onto the sample surface. (b) TEY NEXAFS spectra of the LLDPE film (100 nm) on the silicon substrate with varying angle of X-ray incidence. (c) Summary of dichroic ratio (DR) dependence on incident angle for the spectra in part b. DR is defined as $(I_{287.5\text{eV}} - I_{288.2\text{eV}})/(I_{287.5\text{eV}} + I_{288.2\text{eV}})$.

chain, the trend suggests that the C−C bonds are perpendicular to the fibril. (2) For the split peaks of ~288 eV, the ratio $I_{287.5\text{eV}}/I_{288.2\text{eV}}$ is high at $\Phi = 0°$ and decreases with increasing Φ, reaching the minimum when $\Phi = 90°$. The ratios $I_{292.8\text{eV}}/I_{288.2\text{eV}}$ and $I_{287.5\text{eV}}/I_{288.2\text{eV}}$ are plotted as a function of Φ in Figure 4c, which indeed shows a monotonic increase and monotonic decrease, respectively. As previously concluded based on the data shown in Figure 3, the *a* axis orients mostly perpendicular to the film plane; indeed, the in plane rotation does not affect the $I_{288.2\text{eV}}$ significantly, and the $I_{287.5\text{eV}}/I_{288.2\text{eV}}$ difference is mainly due to the change of $I_{287.5\text{eV}}$. Combining with the results found in previous studies that $I_{287.5\text{eV}}$ maximizes when $\mathbf{E} \parallel b$, we can suggest that the *b* axis lies mostly along the fibril direction. Similarly, the change in $I_{292.8\text{eV}}/I_{288.2\text{eV}}$ is mainly due to the orientation change of the *c* axis, and the tendency confirms that the *c* axis lies mostly in the film plane and perpendicular to the fibril's direction.

Although more systematic study is absolutely needed in order to completely elaborate the precise three-dimensional orientation of the crystal lattice, the above qualitative results are significant. First, from Figure 3, we know *b* and *c* orient mostly in the film plane, while *a* tends to lie along the film plane normal; then from Figure 4, we can suggest that the *b* axis mostly lies along the fibril direction, and the *c* axis lies mostly in the film plane and perpendicular to the fibril's direction. Putting these conclusions together, we propose the following approximate orientation of the crystal unit cell in annealed films: *b* and *c* orient predominantly in the film plane, with *c* perpendicular to the fibril direction, *b* along the fibril direction, and *a* perpendicular to the film plane. The suggested crystallite orientation is shown in Figure 5.

Chain Orientation Study for the LLDPE Films on Mica Substrate. In order to investigate the annealing effect on the crystallization, as-cast and isothermally crystallized 366 nm thick LLDPE films on mica substrates were studied. STXM images of the films are shown in Figure 6. In the as-cast film, loosely packed thin fibril bundles branch from the spherulite center. In the annealed film, however, big spherulite centers are surrounded by bands of rings, which resemble the concentric bands around the spherulite observed under the cross-polarized optical microscopy.[43]

In Figure 7, transmission NEXAFS spectra were acquired by scanning a line repeatedly at a series of different energies, and spectra are thus recorded from the sample areas defined by the line.[42]

Parts a and b of Figure 7 are the spectra of the as-cast film and the film isothermally crystallized, respectively; the green graph in Figure 7b is the reference spectrum for PE from a highly crystalline, nonoriented bulk sample. Different segments of the NEXAFS line spectrum are represented by spectra displayed in different colors. We can see that, even in one sample, the spectra at slightly different areas vary, due to the inhomogeneous thickness and the variations in chain orientation. The spectra in Figure 7b have been intensity normalized for ease of comparison. However, comparing parts a and b, one trend is very obvious: the intensity ratio $I_{292.8\text{eV}}/I_{288\text{eV}}$ in the annealed film is far greater than that in the as-cast film. Since the absorption $I_{292.8\text{eV}}$ is maximized when $\mathbf{E}$ is parallel to the C−C backbone, while, at 288 eV, absorption is maximized with $\mathbf{E}$ aligned in the C−H direction (which is perpendicular to the C−C bonds), and since $\mathbf{E}$ is in the plane of the film, an increase of the ratio $I_{292.8\text{eV}}/I_{288\text{eV}}$ from the as-cast state to the annealed state indicates a tendency of the C−C backbone to be oriented more parallel to the film surface after annealing. In contrast, the very low $I_{292.8\text{eV}}/I_{288\text{eV}}$ for as-cast films is reminiscent of the spectra by Zou et al. on oriented alkane crystals and indicates predominant orientation of the C−C backbone along the surface normal.[25]

To further investigate the morphology and chain orientation in the annealed film, the AFM images of this sample are shown in Figure 8.

The height image of the annealed film is shown in Figure 8a, where we see big spherulites with circular rings around the nucleation centers, which agree with the STXM image in Figure 6b. The square box in Figure 8a is zoomed-in to observe the fine feature. Figure 8b is the lateral force image of the square box, which reflects the surface friction. From this image, we can see rather homogeneous friction across the whole surface. As the amorphous parts have much higher surface friction than the crystalline parts, the lack of friction contrast indicates that the whole film surface is crystallized and that the band morphology is solely due to the height difference. More importantly, the big groove between the spherulite boundary (marked with a dashed line) is completely invisible in the friction image, which indicates that the groove is not the amorphous region but rather there are crystalline polymers beneath the surface gap.

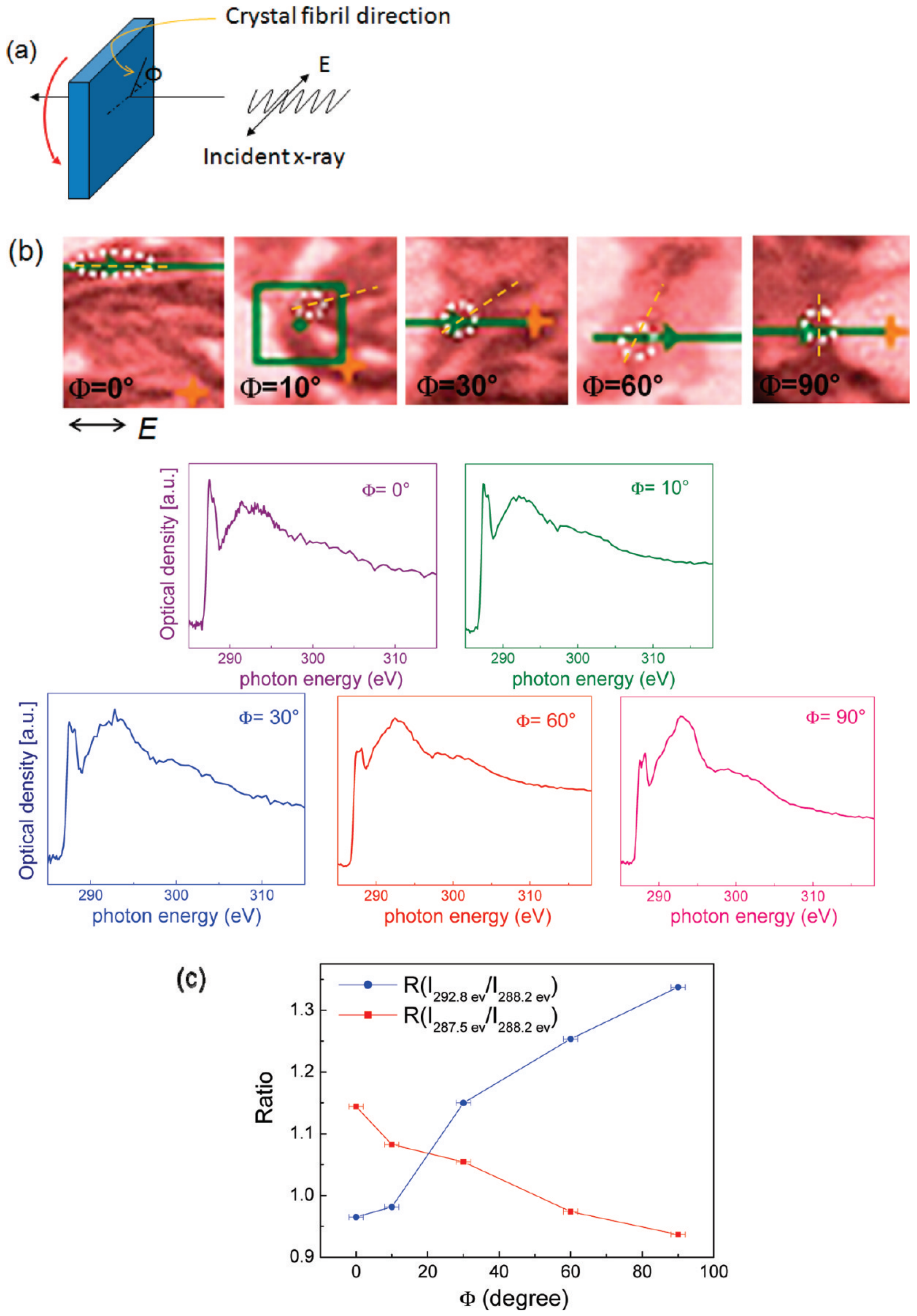

Figure 4. In-plane crystallite orientation measurement by varying the angle between the crystal fibril and the electric field vector. (a) Scheme of the measure geometry. (b) STXM images and the transmission NEXAFS optical density [$-\ln(I/I_0)$] spectra of the LLDPE film with varying Φ, where I_0 is the incident intensity and I is the transmitted intensity. The images were taken at the energy of the first resonance (287.5 eV). In the STXM images, **E** is in the horizontal direction, and the yellow dot marks the location where an image focusing has been done; either a green line or a green square box shows the measuring area (in line measurement or area stack measurement). Only the portion inside the white circle is used to extract a spectrum. The golden dashed line highlights the crystal fibril direction. (c) Summary of the intensity ratios $I_{287.5\text{eV}}/I_{288.2\text{eV}}$ and $I_{292.8\text{eV}}/I_{288.2\text{eV}}$ as a function of Φ for the spectra in part b.

This hypothesis is then verified with the zoomed-in height image and section analysis of the same region (Figure 8c), where the average band spacing is measured to be 837 ± 57 nm, and the average height of the bumps of the bands is 30.06 ± 6.1 nm, while the depth of the groove between the spherulite boundaries is 56.84 ± 6.58 nm. Since the depth of the groove is far smaller than the film thickness (366 nm), we can conclude that there is more than one layer of lamellae. Traditionally, there are two explanations to the origins of the banded structure.[43] One is due to the concentration discontinuity caused by the rhythmic crystal growth;[44,45] the other is the orientation change of the polymer chains caused by the lamellar twisting along the spherulite direction.[46,47] The latter one has proven to be the formation mechanism of the banded morphology in many polymer systems. The height measurements from the section image in our case also support the lamellar twisting model. As shown in Figure 8d, the height of the bumps represents the twisting radius R, while the height of the whole lamellar layer is $2R$. The groove depth (56.84 ± 6.58 nm) resembles the diameter of the twisted lamellae, which is quite close to twice the bump height (30.06 ± 6.1 nm).

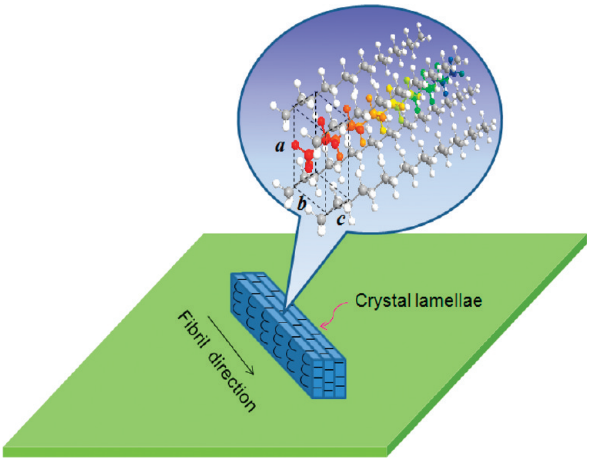

Figure 5. Schematic representation of the suggested crystal unit cell orientation with respect to the crystal lamellae, the fibril direction, and the substrate.

To probe the chain orientation in order to see if the lamellar twisting is the mechanism for the band morphology, NEXAFS optical density (OD) images acquired at the C-1s → $\sigma^*_{\mathrm{C-H}}$ energy and the C-1s → $\sigma^*_{\mathrm{C-C}}$ energy are shown in Figure 9.

The origin of the X-ray contrast is given by eq 1:[16]

$$I = I_0 \exp(-\mu\rho t) \tag{1}$$

where I is the transmitted intensity, I_0 is the incident photo flux intensity, μ is the mass absorption coefficient, and ρ is the density. The optical density that represents X-ray adsorption spectra is defined as

$$\mathrm{OD} = -\ln(I/I_0) = \mu\rho t \tag{2}$$

In multicomponent systems, OD at a certain energy is the summation of the contribution from all the components i:

$$\mathrm{OD}_{\mathrm{Er}} = \sum_{i=1}^{n} \mu_i^{\mathrm{Er}} \rho_i t_i \tag{3}$$

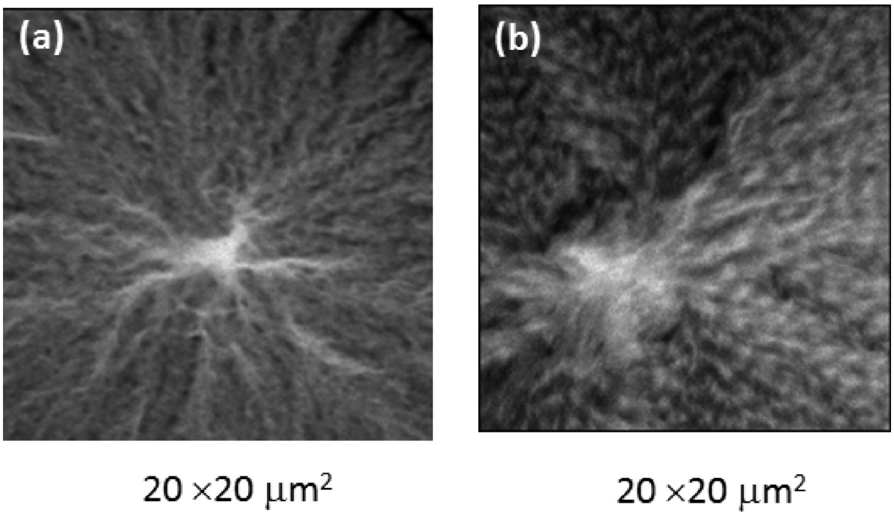

20 ×20 μm²

20 ×20 μm²

Figure 6. STXM images of LLDPE film (366 nm) crystallized on mica substrate: (a) as-cast; (b) isothermally crystallized at 60 °C.

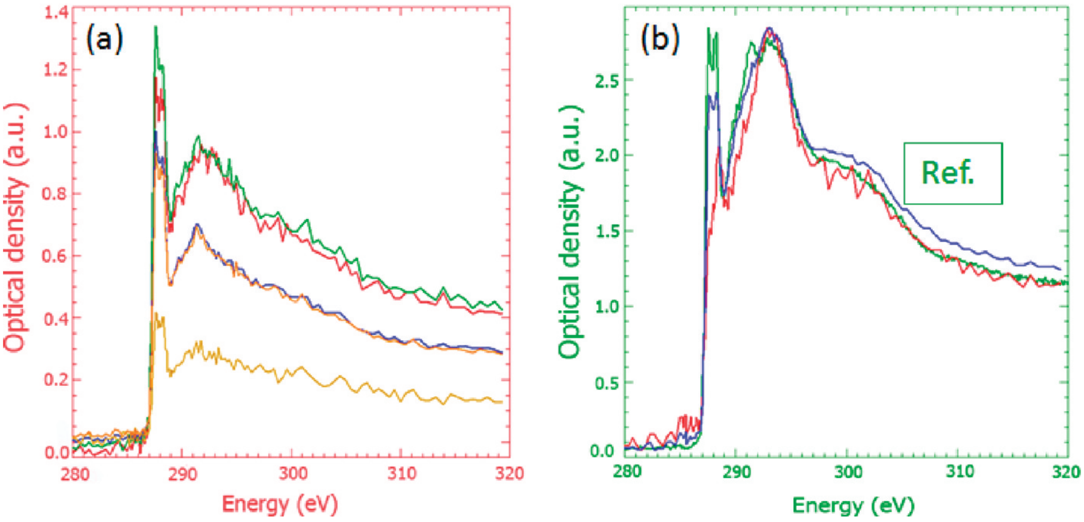

Figure 7. Transmission NEXAFS optical density spectra of a line scan image of a 366 nm thick LLDPE film crystallized on mica. The curves with different colors are from different sample locations along a line. The overall intensity differences thus reflect the variation in the film thickness: (a) as-cast; (b) isothermally crystallized. The green curve in part b is the reference spectrum of bulk PE. Spectra in part b have been normalized for easier comparison.

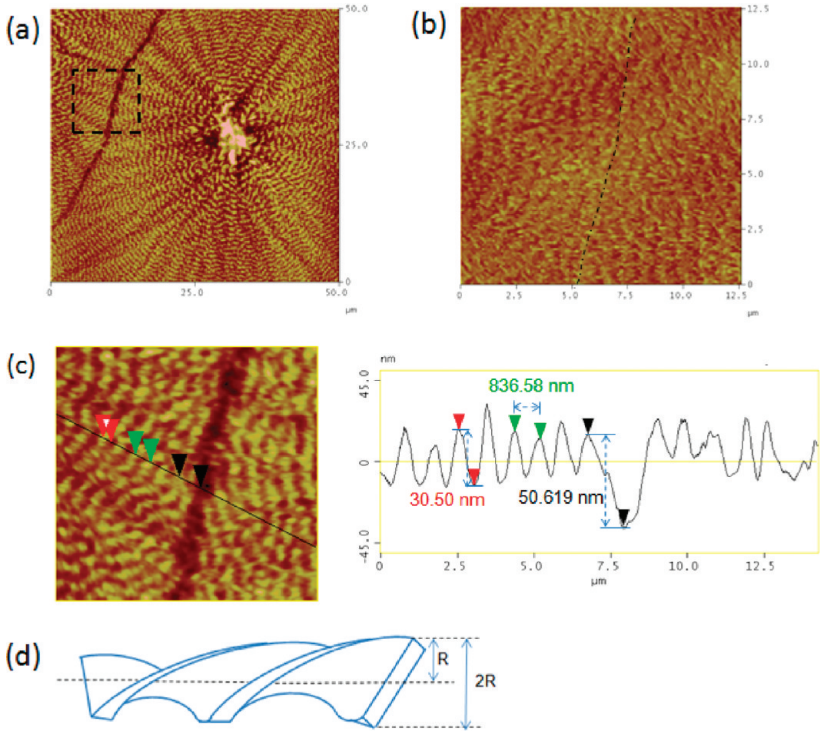

Figure 8. AFM images of isothermally crystallized LLDPE film (366 nm) on mica. (a) Height image of film with scan size 50 × 50 μm^2. (b) Zoom-in lateral force image of the square box in part a. (c) Zoom-in height image of the square box in part a, with the section analysis. (d) Schematic drawing of the twisted lamellar geometry.

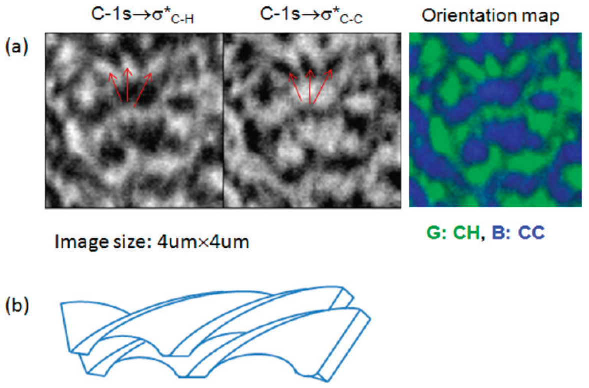

Figure 9. (a) Optical density (OD) images and singular value decomposition (SVD) fitting of isothermally crystallized LLDPE film (366 nm) on a mica substrate. The left column is the OD image taken at C-1s → $\sigma^*_{\mathrm{C-H}}$ energy. The middle column is the OD image taken at C-1s → $\sigma^*_{\mathrm{C-C}}$ energy. The arrows highlight the same areas with reverse brightness in the two images. The right image is the quasi-compositional, i.e., orientation, map obtained from SVD fitting. (b) Schematic drawing of multilayer lamellar structure and orientation.

For a component with a specific absorption energy, μ_i^{Er} for this component is very large at this specific energy, and as a consequence, in the OD map taken at this energy, the areas that are rich with this component have a far greater OD than the areas that are low of this component. In our case, there is only one composition; however, since **E** is parallel to the film plane, the orientation of the chains results in different absorption of the X-ray. So the regions where C−C is lateral to the film plane act as the C−C rich regions, while regions for which C−H is in the film plane act as the C−H rich regions. Based on the fact that the density is uniform regardless of the orientation and C-1s → $\sigma^*_{\mathrm{C-C}}$(~293 eV) and C-1s → $\sigma^*_{\mathrm{C-H}}$(288 eV) are the characteristic absorption peaks when **E**∥C−C chain or **E**⊥C−C chain, the OD images acquired at these two energies reflect the orientation distribution. The quasi-compositional maps that reflect orientations can be obtained with singular value decomposition (SVD) fitting, where the relative concentration of different compositions can be shown in one map.[32] The OD images acquired at the C−H energy and the C−C energy as well as the quasi-compositional map of the annealed film are shown in Figure 9. From the figure it is seen clearly that there is an inhomogeneity of the C−H and C−C distribution, which is in agreement with the lamellar twisting model that the C−C lateral and C−H lateral orientations alternate along the spherulite radiation direction; when the chains are parallel to the surface, there is a stronger C-1s → $\sigma^*_{\mathrm{C-C}}$ absorption and a weaker C-1s → $\sigma^*_{\mathrm{C-H}}$ absorption, and vice versa. The arrows highlight the same areas in the film, with reverse brightness in the different OD images, which are the C−H rich regions, i.e., the C−H in the film plane. The quasi-compositional map in the right column demonstrates the orientation distribution. However, one puzzle remains: since the films are composed of more than one lamellae layer, and the OD images reflect the information of the summation from all the layers, the compositional map demonstrates that the chain orientation distributions at the same spot are the same or very similar for all the layers. More systematic studies are required to thoroughly elaborate the origin, the mechanism, and the geometry of the lamellar construction; here, we propose the possibility of the epitaxial alignment of the lamellae from layer to layer, where the lamellae in different layers follow the orientation of that in the previous layer, as shown in Figure 9b. The groove at the spherulite borders represents the impingement of the first layer lamellae, while the layer underneath is continuous at these areas, resulting in a homogeneous friction image.

The different morphologies and the chain orientations of PE on silicon and mica substrates can be explained by the difference in their interfacial interactions. The affinity

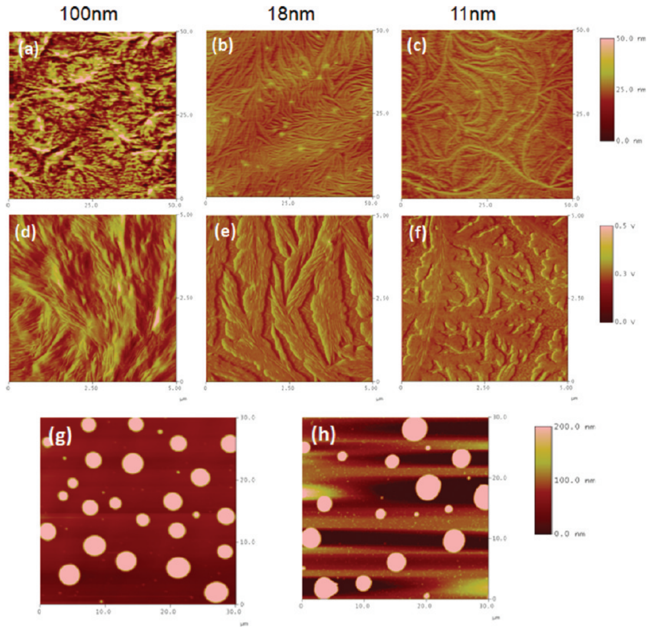

Figure 10. AFM height images of LLDPE films with different thicknesses on silicon and on mica substrates, isothermally crystallized. First row: (a−c) height images of films on silicon with scan size of 50 × 50 μm^2. Second row: (d−f) Lateral force images of the same films in the first row with scan size of 5 × 5 μm^2. Third row: films on mica substrate: (g) 180 nm thick film; (h) 30 nm thick film.

between the liquid and solid substrates can be determined by the interfacial energy γ_{sl}, which can be calculated using the Owens−Wendt−Kaelble equation:[48]

$$\gamma_{ls} = \gamma_l + \gamma_s - 2(\gamma_s^d \gamma_l^d)^{1/2} - 2(\gamma_s^p \gamma_l^p)^{1/2} \qquad (5)$$

in which γ_s^d and γ_s^p are the dispersion and polar parts of the surface energy of the solid, while γ_l^d and γ_l^p are the dispersion and polar parts of the surface energy of the liquid phase.

Since, in the crystallization process, PE film was first heated to a temperature above its bulk T_m, it can be viewed as a liquid phase in the above calculation. For silicon, γ_s^d and γ_s^p are 48.71 mJ/m^2 and 3.98 mJ/m^2, respectively.[2,6] For mica, γ_s^d and γ_s^p are 30 mJ/m^2 and 90 mJ/m^2 respectively,[49,50] while, for PE, γ_l^d and γ_l^p are 30 mJ/m^2 and 0, respectively.[51] Using eq 5 to calculate the interfacial energy, we obtained $\gamma_{PE/Si}$ = 5.6 mJ/m^2 and $\gamma_{PE/mica}$ = 90 mJ/m^2, indicating the silicon has a much stronger attraction to PE than mica does to PE. As we crystallized the films on silicon and mica with different thermal conditions (nonisothermal crystallization on silicon and isothermal crystallization on mica), we want to rule out the possibility that the different annealing methods are the key role to induce the different crystallization features on these two substrates. In Figure 10, the morphologies of the films crystallized isothermally at 60 °C on silicon substrates are compared with those crystallized on mica with the same annealing method.

On the silicon, the morphology dependence on film thickness is quite similar to those with nonisothermal crystallization which we have shown in detail in our previous study:[5] For the 100 nm thick film, we see compact spherulites with mostly edge-on lamellae; in the 18 nm film, the crystals exhibit hedrite branching structure, and the packing of the lamellar is less dense; in the 11 nm film, sparser dendritic crystallites are observed, with the flat-on lamellae dominant. On the mica substrate, however, except for the 366 nm thick film, the morphology of which was shown in Figure 8, films with thickness of 180 nm or less completely dewet and form isolated droplets on the substrate. This is an evidence of the weak adsorption of LLDPE to the mica.

From the above results, it can be concluded that for the weak interactive substrate, i.e. mica, the chains orient mostly perpendicular to the substrate in the as-cast films, while chain reorientation occurs in the thick film during the annealing process, after which lamellar twisting is observed. This observation is consistent with the high interfacial energy between the polymer and the substrate. In the as-cast film, the quick cooling process does not allow the crystal to reach an equilibrium structure, and the chains naturally take the perpendicular position to minimize the contact with the substrate; after being crystallized overnight, more mature crystals are grown and lamella twisting happens. As the twisted lamellae are generally observed in the bulk polymers or polymer thick films where there is no or very little influence of the substrate, we can see that mica substrate posts very little or nearly no effect on LLDPE crystallization, while the chain orientation on the silicon substrate is a result of the strong LLDPE/substrate attraction. A further important note on the LLDPE/silicon attraction is that although the attraction force is strong enough to keep the films from dewetting and to affect the orientation of the crystal lamellae and the polymer chain, as has been demonstrated both in this report and in our previous studies,[5] we believe that there is no chemical adsorption and the attraction force is not strong enough to permanently pin the molecules onto the substrate, as the films could be lifted off the silicon substrate and transferred onto the transparent grid for TEM measurement[5] or NEXAFS measurement in transmission mode.

Conclusions

NEXAFS has proven to be very sensitive to the chain and crystal lattice orientation of the PE thin films. By measuring the LLDPE thin films on different substrates and with different thermal histories, the following conclusions have been reached:

1. In the nonisothermally crystallized films that are 100 nm thick on the silicon substrate, the backbone chains orient mainly parallel to the substrate.
2. Within the crystal fibrils, the approximate average orientation of the orthorhombic unit cell is suggested to be as follows: *c* and *b* in the film plane with *c* orientated perpendicular to the fibril direction and *b* along the fibril direction; *a* is perpendicular to the film plane.
3. On a weakly interactive substrate, i.e. mica, the crystal morphology and orientation in the 366 nm thick film before and after annealing are compared. In the as-cast films, crystals are not in the equilibrium state, and the chains tend to take a perpendicular orientation to avoid contact with the substrate; after isothermal crystallization, lamellar twisting happens, more than one layer of the twisted lamellae exists in the film, and all the layers follow the same orientation at a certain area. For the films thinner than 180 nm, complete dewetting occurs after annealing.
4. Different annealing methods are not the cause of the difference in morphologies and chain orientation of the LLDPE on the two different substrates in this study, as the isothermally crystallized LLDPE on the silicon shows very similar morphologies to the nonisothermally crystallized LLDPE,[5] and a film as thin as 11 nm crystallizes as very nice flat-on lamellae over the entire substrate.

Acknowledgment. The authors wish to thank Dr. Arnold Lustiger at ExxonMobil Research and Engineering Corporation for providing the polyethylene. The X-ray characterization work by NCSU is supported by the U.S. Department of Energy, Office of Science, Basic Energy Science, Division of Materials Science and Engineering, for support under Contract DE-FG02-98ER45737. We acknowledge beamline BL-5-2 at Stanford Synchrotron Radiation Lightsource and beamline 5.3.2 at the Advanced Light Source at Lawrence Berkeley National Laboratory for providing the instrumentation and beam time for the NEXAFS and STXM experiments, respectively.

References and Notes

(1) Marzantowicz, M.; Dygas, J. R.; Krok, F. *Electrochim. Acta* **2008**, *53*, 7417–7425.
(2) Sommer, M.; Huttner, S.; Steiner, U.; Thelakkat, M. *Appl. Phys. Lett.* **2009**, *95*, 3.
(3) Amendola, E.; Cammarano, A.; Pezzuto, M.; Acierno, D. *J. Eur. Opt. Soc.—Rapid Publ.* **2009**, 4.
(4) Wallner, G. M.; Lang, R. W. *Sol. Energy* **2005**, *79*, 603–611.
(5) Wang, Y.; Ge, S.; Rafailovich, M.; Sokolov, J.; Zou, Y.; Ade, H.; Luning, J.; Lustiger, A.; Maron, G. *Macromolecules* **2004**, *37*, 3319–3327.
(6) Wang, Y.; Rafailovich, M.; Sokolov, J.; Gersappe, D.; Araki, T.; Zou, Y.; Kilcoyne, A. D. L.; Ade, H.; Marom, G.; Lustiger, A. *Phys. Rev. Lett.* **2006**, *96*, 028303.
(7) Wunderlich, B. *Macromolecular Physics*; Academic Press: New York, 1973.
(8) Hannay, N. B. *Treatise on Solid State Chemistry*; Plenum Press: New York, 1976; Vol. *3*.
(9) Despotopoulou, M. M.; Miller, R. D.; Rabolt, J. F.; Frank, C. W. *J. Polym. Sci., Polym. Phys.* **1996**, *34*, 2335–2349.
(10) Ho, P. K. H.; Chua, L. L.; Dipankar, M.; Gao, X. Y.; Qi, D. C.; Wee, A. T. S.; Chang, J. F.; Friend, R. H. *Adv. Mater.* **2007**, *19*, 215+.
(11) Sambasivan, S.; Hsieh, S.; Fischer, D. A.; Hsu, S. M. *J. Vac. Sci. Technol., A* **2006**, *24*, 1484–1488.
(12) Hemraj-Benny, T.; Banerjee, S.; Sambasivan, S.; Balasubramanian, M.; Fischer, D. A.; Eres, G.; Puretzky, A. A.; Geohegan, D. B.; Lowndes, D. H.; Han, W. Q.; Misewich, J. A.; Wong, S. S. *Small* **2006**, *2*, 26–35.
(13) Hu, W. S.; Lin, Y. F.; Tao, Y. T.; Hsu, Y. J.; Wei, D. H. *Macromolecules* **2005**, *38*, 9617–9624.
(14) Kondoh, H.; Nambu, A.; Ehara, Y.; Matsui, F.; Yokoyama, T.; Ohta, T. *J. Phys. Chem. B* **2004**, *108*, 12946–12954.
(15) Samant, M. G.; Stohr, J.; Brown, H. R.; Russell, T. P.; Sands, J. M.; Kumar, S. K. *Macromolecules* **1996**, *29*, 8334–8342.
(16) Fu, J.; Urquhart, S. G. *Langmuir* **2007**, *23*, 2615–2622.
(17) Pattison, L. R.; Hexemer, A.; Kramer, E. J.; Krishnan, S.; Petroff, P. M.; Fischer, D. A. *Macromolecules* **2006**, *39*, 2225–2231.
(18) Bierbaum, K.; Kinzler, M.; Woll, C.; Grunze, M.; Hahner, G.; Heid, S.; Effenberger, F. *Langmuir* **1995**, *11*, 512–518.
(19) Hahner, G.; Woll, C.; Buck, M.; Grunze, M. *Langmuir* **1993**, *9*, 1955–1958.
(20) Ouchi, Y.; Mori, I.; Sei, M.; Ito, E.; Araki, T.; Ishii, H.; Seki, K.; Kondo, K. *Physica B* **1995**, *208*, 407–408.
(21) Weiss, K.; Bagus, P. S.; Woll, C. *J. Chem. Phys.* **1999**, *111*, 6834–6845.
(22) Stohr, J.; Outka, D. A.; Baberschke, K.; Arvanitis, D.; Horsley, J. A. *Phys. Rev. B* **1987**, *36*, 2976–2979.
(23) Ohta, T.; Seki, K.; Yokoyama, T.; Morisada, I.; Edamatsu, K. *Phys. Scr.* **1990**, *41*, 150–153.
(24) Scholl, A.; Fink, R.; Umbach, E.; Mitchell, G. E.; Urquhart, S. G.; Ade, H. *Chem. Phys. Lett.* **2003**, *370*, 834–841.
(25) Zou, Y.; Araki, T.; Appel, G.; Kilcoyne, A. L. D.; Ade, H. *Chem. Phys. Lett.* **2006**, *430*, 287–292.
(26) Ade, H.; Hsiao, B. *Science* **1993**, *262*, 1427–1429.
(27) Smith, A. P.; Ade, H. *Appl. Phys. Lett.* **1996**, *69*, 3833–3835.
(28) Castner, D. G.; Lewis, K. B.; Fischer, D. A.; Ratner, B. D.; Gland, J. L. *Langmuir* **1993**, *9*, 537–542.
(29) Lippitz, A.; Friedrich, J. F.; Unger, W. E. S.; Schertel, A.; Woll, C. *Polymer* **1996**, *37*, 3151–3155.
(30) Weiss, K.; Woll, C.; Bohm, E.; Fiebranz, B.; Forstmann, G.; Peng, B.; Scheumann, V.; Johannsmann, D. *Macromolecules* **1998**, *31*, 1930–1936.
(31) Weiss, K.; Woll, C.; Johannsmann, D. *J. Chem. Phys.* **2000**, *113*, 11297–11305.
(32) Ade, H.; Hitchcock, A. P. *Polymer* **2008**, *49*, 643–675.
(33) Rousseau, M. E.; Cruz, D. H.; West, M. M.; Hitchcock, A. P.; Pezolet, M. *J. Am. Chem. Soc.* **2007**, *129*, 3897–3905.
(34) Sambasivan, S.; Fischer, D. A.; Shen, M. C.; Hsu, S. M. *J. Biomed. Mater. Res., Part B* **2004**, *70B*, 278–285.
(35) Zhang, X. D.; Balhorn, R.; Mazrimas, J.; Kirz, J. *J. Struct. Biol.* **1996**, *116*, 335–344.
(36) Rightor, E. G.; Hitchcock, A. P.; Ade, H.; Leapman, R. D.; Urquhart, S. G.; Smith, A. P.; Mitchell, G.; Fischer, D.; Shin, H. J.; Warwick, T. *J. Phys. Chem. B* **1997**, *101*, 1950–1960.
(37) Dhez, O.; Ade, H.; Urquhart, S. G. *J. Electron Spectrosc. Relat. Phenom.* **2003**, *128*, 85–96.
(38) Young, R. J.; Lovell, P. A. *Introduction to Polymers*; Chapman & Hall: London, 1991.
(39) Simanke, A. G.; Alamo, R. G.; Galland, G. B.; Mauler, R. S. *Macromolecules* **2001**, *34*, 6959–6971.
(40) Stöhr, J. *NEXAFS Spectroscopy*; Springer-Verlag: Berlin, Heidelberg, 1992.
(41) Shin, K.; Hu, X.; Zheng, X.; Rafailovich, M. H.; Sokolov, J.; Zaitsev, V.; Schwarz, S. A. *Macromolecules* **2001**, *34*, 4993–4998.
(42) Kilcoyne, A. L. D.; Tyliszczak, T.; Steele, W. F.; Fakra, S.; Hitchcock, P.; Franck, K.; Anderson, E.; Harteneck, B.; Rightor, E. G.; Mitchell, G. E.; Hitchcock, A. P.; Yang, L.; Warwick, T.; Ade, H. *J. Synchrotron Radiat.* **2003**, *10*, 125–136.
(43) Wang, T. C.; Wang, H. J.; Li, H. H.; Gan, Z. H.; Yan, S. K. *Phys. Chem. Chem. Phys.* **2009**, *11*, 1619–1627.
(44) Keith, H. D.; Padden, F. J. *J. Polym. Sci.* **1959**, *39*, 123–138.
(45) Keith, H. D.; Padden, F. J. *Macromolecules* **1996**, *29*, 7776–7786.
(46) Price, F. P. *J. Polym. Sci.* **1959**, *39*, 139–150.
(47) Keller, A. *J. Polym. Sci.* **1959**, *39*, 151–173.
(48) Kwok, D. Y.; Neumann, A. W. *Adv. Colloid Interface Sci.* **1999**, *81*, 167–249.
(49) Schultz, J.; Tsutsumi, K.; Donnet, J. B. *J. Colloid Interface Sci.* **1977**, *59*, 272–276.
(50) Schultz, J.; Tsutsumi, K.; Donnet, J. B. *J. Colloid Interface Sci.* **1977**, *59*, 277–282.
(51) Wu, S. *J. Macromol. Sci., Rev. Macromol. Chem. Phys.* **1974**, *C10*, 1–73.